Design and Control of a Passively Morphing Quadcopter

Nathan Bucki and Mark W. Mueller

Abstract— **This paper presents a novel quadcopter design that uses passive rotary joints to enable rapid aerial morphing without the use of additional actuators. The normally rigid connections between the arms of the quadcopter and the central body are replaced by sprung hinges that allow for the arms of the quadcopter to fold downward when low thrusts are produced by the propellers, resulting in a reduction of the largest dimension of the vehicle by approximately 50%. The ability of the vehicle to reduce its size during flight allows, e.g., for the traversal of gaps through which a non-morphing quadcopter could not pass. The vehicle is designed such that existing quadcopter controllers and trajectory generation algorithms can be used, provided that some additional constraints on the control inputs are met. The nonlinear dynamics of the system are presented, and design rules are given that minimize transition time between configurations and maximize the available range of control inputs. A method for performing gap traversal maneuvers is proposed and validated experimentally.**

I. Introduction

Quadcopters are able to perform highly agile maneuvers, allowing for the rapid traversal of dense indoor environments [1]. As exhibited in [2], such high speed navigation often requires the ability to accurately track trajectories through narrow gaps. The ability of a quadcopter to traverse narrow gaps was further explored in [3], which showed how a quadcopter can accurately perform gap crossing maneuvers using only onboard sensing.

Several quadcopter based vehicles have been designed for the purpose of flight through small apertures, all of which use additional actuators to change the configuration of the vehicle during flight. These include a vehicle that uses several servomotors to actuate a scissor-like structure that can shrink or expand the size of the vehicle as presented in [4], a quadcopter that uses a single servomotor to change the angle of its arms in an X-shape as presented in [5], a quadcopter that can tilt its propellers to enter a vertical flying mode configuration for passage through narrow areas as presented in [6], a quadcopter that uses a single servomotor to rotate the position of its propellers in order to dramatically reduce the wingspan of the vehicle as presented in [7], and a quadcopter with tilting propellers that allows for fully-actuated flight by adding four additional servomotors as presented in [8].

The vehicle proposed here differs from other actively morphing quadcopter-based aerial vehicles in that it does not use any actuators beyond the four motors used to spin the propellers to change the shape of the vehicle. Springs are used to pull the arms into the folded configuration, which occurs when the thrust forces drop below a certain threshold governed by the torques exerted by the springs about the hinges. During regular flight, the thrust forces produced by the propellers are high enough to keep the arms unfolded, allowing the vehicle to function as a normal quadcopter. Furthermore, the dynamics of the vehicle in the unfolded configuration match those of a standard quadcopter, allowing for the use of existing quadcopter controllers and trajectory generation techniques given that the thrust forces of each propeller remain high enough to keep the vehicle in the unfolded configuration.

The authors are with the High Performance Robotics Lab, University of California, Berkeley, CA 94703, USA. {nathan_bucki, mwm}@berkeley.edu

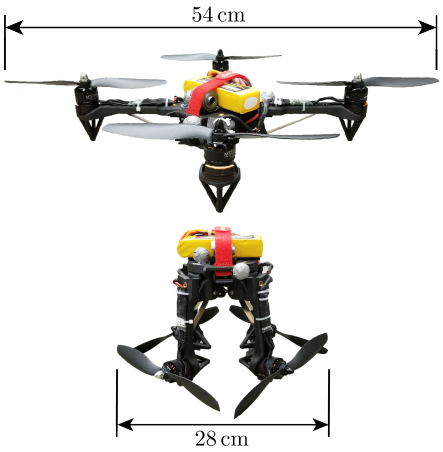

Fig. 1. Experimental vehicle in the unfolded (top) and folded (bottom) configurations. The vehicle changes shape without the use of any additional actuators. When low thrust forces are produced by the propellers, springs pull the arms downward into the folded configuration. When high thrust forces are produced, the vehicle transitions into the unfolded configuration.

Figure 1 shows the vehicle in the unfolded and folded configurations. The design of our vehicle is inspired in part by how birds fold their wings when passing through narrow gaps, as shown in [9]. The use of bioinspired morphing wings was explored in [10], which showed how morphing wings can use aerodynamic effects to improve maneuverability.

A self-deploying quadcopter was presented in [11] which uses foldable origami-style arms to automatically increase its wingspan during takeoff. Our vehicle differs from the vehicle presented in [11] by enabling repeated changes of shape during flight rather than a single shape change during takeoff. The ability of our vehicle to significantly reduce its size also allows for it to be transported compactly, and the use of passive rotary joints allows for rapid deployment with minimal user interference.

II. System Overview

In this section we define a model of the system and derive the dynamics of the vehicle. The vehicle consists of four rigid arms connected to a central body via unactuated rotary joints. The joints are limited to a range of motion of approximately $90°$. Constant-force linear springs are used to provide the force necessary to transition to the folded configuration, and the thrust forces produced by the propellers are used to keep the vehicle in the unfolded configuration.

A. Notation

Non-bold symbols such as m represent scalars, lowercase bold symbols such as $\boldsymbol{g}$ represent first order tensors (vectors), and uppercase bold symbols such as $\boldsymbol{J}$ represent second order tensors (matrices). The short-hand notation (x, y, z) represents a column vector. Subscripts such as m_B represent the body to which the symbol refers, and superscripts such as $\boldsymbol{g}^E$ represent the frame in which the tensor is expressed. A second subscript or superscript such as $\boldsymbol{\omega}_{BE}$ or $\boldsymbol{R}^{BE}$ represents what the quantity is defined with respect to. The symbol $\boldsymbol{d}$ represents a displacement, $\boldsymbol{\omega}$ represents an angular velocity, and $\boldsymbol{R}$ represents a rotation matrix. The skew-symmetric matrix form of the cross product is written as $S(\boldsymbol{a})$ such that $S(\boldsymbol{a})\boldsymbol{b} = \boldsymbol{a} \times \boldsymbol{b}$.

B. Model

The system is modeled as five coupled rigid bodies: the four arms and the central body of the vehicle. Figure 2 shows the internal and external forces and torques acting on a single arm and the central body. The body-fixed frame B is defined to be at the center of mass of the central body, and the arm-fixed frame A_i is defined to be at the center of mass of arm i. A_1, A_2, A_3, and A_4 are defined to lie in the $\boldsymbol{x}_B$, $-\boldsymbol{y}_B$, $-\boldsymbol{x}_B$, and $\boldsymbol{y}_B$ directions respectively. The inertial frame is notated by E, and H_i refers to the location of hinge i. Constant force spring i is connected between point S_i on the central body and point M_i on arm i, and produces spring force $\boldsymbol{f}_{s_i}$. The rotation matrix of frame B with respect to frame E is defined as $\boldsymbol{R}^{BE}$ such that the quantity $\boldsymbol{v}^B$ expressed in the B frame is equal to $\boldsymbol{R}^{BE}\boldsymbol{v}^E$ where $\boldsymbol{v}^E$ is the same quantity expressed in frame E. The orientation of arm i with respect to the central body is defined through the single degree of freedom rotation matrix $\boldsymbol{R}^{A_iB}$.

The internal reaction forces and torques acting at the hinge are defined as $\boldsymbol{f}_{r_i}$ and $\boldsymbol{\tau}_{r_i}$ respectively. The propeller attached to the arm produces thrust force f_{p_i} and torque τ_{p_i} in the $\boldsymbol{z}_{A_i}$ direction. We assume that the torque produced by each propeller is linearly related to the propeller thrust force by $\tau_{p_i} = \kappa_{p_i} f_{p_i}$, where the sign κ_{p_i} is determined by the rotation direction of propeller i [12].

The mass and mass moment of inertia of the central body taken at the center of mass of the central body are denoted m_B and $\boldsymbol{J}_B$ respectively, and the mass and mass moment of inertia of each arm taken at the center of mass of each arm are denoted m_A and $\boldsymbol{J}_A$ respectively. We assume the mass and mass moment of inertia of each arm is equal.

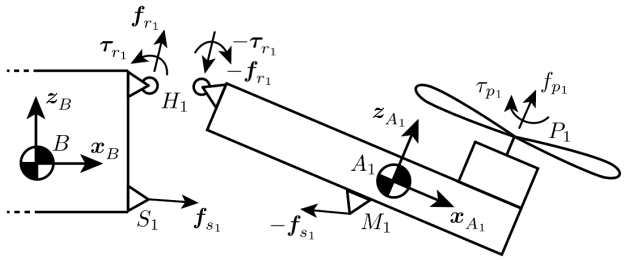

Fig. 2. Free-body diagram showing the forces and torques acting on the central body and arm 1 of the vehicle. An animation of the mechanism can be viewed here: `https://youtu.be/MSvoQT__c9U`

C. Dynamics

The translational and rotational dynamics of the central body of the vehicle and the four arms are found using Newton's second law and Euler's law respectively [13]. The time derivative of a vector is taken in the reference frame of that vector. Displacement vectors are chosen such that they are constant in the reference frame in which they are expressed.

The translational dynamics of the central body are expressed in the inertial frame E, and the rotational dynamics of the central body are expressed in the body-fixed frame B. The translational dynamics of the central body are:

$$m_B \ddot{\boldsymbol{d}}^E_{BE} = m_B \boldsymbol{g}^E + \boldsymbol{R}^{EB} \sum_{i=1}^{4} \left(\boldsymbol{f}^B_{r_i} + \boldsymbol{f}^B_{s_i} \right) \tag{1}$$

The rotational dynamics of the central body are:

$$\begin{aligned} &\boldsymbol{J}^B_B \dot{\boldsymbol{\omega}}^B_{BE} + S(\boldsymbol{\omega}^B_{BE}) \boldsymbol{J}^B_B \boldsymbol{\omega}^B_{BE} \\ &\quad = \sum_{i=1}^{4} \left(\boldsymbol{\tau}^B_{r_i} + S(\boldsymbol{d}^B_{H_iB}) \boldsymbol{f}^B_{r_i} + S(\boldsymbol{d}^B_{BS_i}) \boldsymbol{f}^B_{s_i} \right) \end{aligned} \tag{2}$$

The translational and rotational dynamics of arm i are both expressed in frame A_i. The translational dynamics of arm i are (Note $\boldsymbol{f}^{A_i}_{r_i} = \boldsymbol{R}^{A_iB} \boldsymbol{f}^B_{r_i}$ and $\boldsymbol{f}^{A_i}_{s_i} = \boldsymbol{R}^{A_iB} \boldsymbol{f}^B_{s_i}$):

$$\begin{aligned} &m_A \left(\boldsymbol{R}^{A_iE} \ddot{\boldsymbol{d}}^E_{BE} + \boldsymbol{\alpha} + \boldsymbol{\beta} \right) \\ &\quad = m_{A_i} \boldsymbol{R}^{A_iE} \boldsymbol{g}^E + \boldsymbol{z}^{A_i}_{A_i} f_{p_i} - \boldsymbol{f}^{A_i}_{r_i} - \boldsymbol{f}^{A_i}_{s_i} \end{aligned} \tag{3}$$

where $\boldsymbol{\alpha}$ and $\boldsymbol{\beta}$ are defined as:

$$\boldsymbol{\alpha} = \boldsymbol{R}^{A_iB} \left(S(\boldsymbol{d}^B_{BH_i}) \dot{\boldsymbol{\omega}}^B_{BE} + S(\boldsymbol{\omega}^B_{BE}) S(\boldsymbol{d}^B_{BH_i}) \boldsymbol{\omega}^B_{BE} \right) \tag{4}$$

$$\boldsymbol{\beta} = S(\boldsymbol{d}^{A_i}_{H_iA_i}) \dot{\boldsymbol{\omega}}^{A_i}_{A_iE} + S(\boldsymbol{\omega}^{A_i}_{A_iE}) S(\boldsymbol{d}^{A_i}_{H_iA_i}) \boldsymbol{\omega}^{A_i}_{A_iE} \tag{5}$$

The rotational dynamics of arm i are ($\boldsymbol{\tau}^{A_i}_{r_i} = \boldsymbol{R}^{A_iB} \boldsymbol{\tau}^B_{r_i}$):

$$\begin{aligned} &\boldsymbol{J}^{A_i}_{A_i} \dot{\boldsymbol{\omega}}^{A_i}_{A_iE} + S(\boldsymbol{\omega}^{A_i}_{A_iE}) \boldsymbol{J}^{A_i}_{A_i} \boldsymbol{\omega}^{A_i}_{A_iE} = S(\boldsymbol{d}^{A_i}_{P_iA_i}) \boldsymbol{z}^{A_i}_{A_i} f_{p_i} \\ &\quad + \boldsymbol{z}^{A_i}_{A_i} \tau_{p_i} - \boldsymbol{\tau}^{A_i}_{r_i} - S(\boldsymbol{d}^{A_i}_{H_iA_i}) \boldsymbol{f}^{A_i}_{r_i} - S(\boldsymbol{d}^{A_i}_{M_iA_i}) \boldsymbol{f}^{A_i}_{s_i} \end{aligned} \tag{6}$$

The equations of motion of the arm are written in terms of $\dot{\boldsymbol{\omega}}^{A_i}_{A_iE}$ and $\boldsymbol{\omega}^{A_i}_{A_iE}$ for convenience, which evaluate to:

$$\boldsymbol{\omega}^{A_i}_{A_iE} = \boldsymbol{\omega}^{A_i}_{A_iB} + \boldsymbol{R}^{A_iB} \boldsymbol{\omega}^B_{BE} \tag{7}$$

$$\dot{\boldsymbol{\omega}}^{A_i}_{A_iE} = \dot{\boldsymbol{\omega}}^{A_i}_{A_iB} + \boldsymbol{R}^{A_iB} \dot{\boldsymbol{\omega}}^B_{BE} - S(\boldsymbol{\omega}^{A_i}_{A_iB}) \boldsymbol{R}^{A_iB} \boldsymbol{\omega}^B_{BE} \tag{8}$$

Furthermore, note that the reaction torque acting in the rotation direction of hinge i is zero when arm i is rotating between the folded and unfolded configurations ($\boldsymbol{y}_{A_i}^{A_i} \cdot \boldsymbol{\tau}_{r_i}^{A_i} = 0$), positive when arm i is in the folded configuration ($\boldsymbol{y}_{A_i}^{A_i} \cdot \boldsymbol{\tau}_{r_i}^{A_i} \geq 0$), and negative when arm i is in the unfolded configuration ($\boldsymbol{y}_{A_i}^{A_i} \cdot \boldsymbol{\tau}_{r_i}^{A_i} \leq 0$).

The dynamics are used in Section III-A in order to compute bounds on the control inputs that, when satisfied, guarantee the vehicle will remain in the unfolded configuration.

III. Control

While in the unfolded configuration, a controller similar to those used with standard quadcopters is used (e.g. as in [14]) with only minor modifications. A position controller computes the desired total thrust, $f_\Sigma = \sum_{i=1}^{4} f_{p_i}$, and thrust direction based on position and velocity errors, and an attitude controller computes desired body torques, (τ_x, τ_y, τ_z), required to track the desired thrust direction and desired yaw angle. Individual motor forces necessary to generate the desired total thrust and desired body torques are then computed as follows, where the distance between each thrust axis and the center of mass is $l_{PB} = d_{P_1 B,x}^{B}$.

$$\begin{bmatrix} f_{p_1} \\ f_{p_2} \\ f_{p_3} \\ f_{p_4} \end{bmatrix} = \frac{1}{4} \begin{bmatrix} 1 & 0 & -2l_{PB}^{-1} & \kappa_{p_1}^{-1} \\ 1 & -2l_{PB}^{-1} & 0 & \kappa_{p_2}^{-1} \\ 1 & 0 & 2l_{PB}^{-1} & \kappa_{p_3}^{-1} \\ 1 & 2l_{PB}^{-1} & 0 & \kappa_{p_4}^{-1} \end{bmatrix} \begin{bmatrix} f_\Sigma \\ \tau_x \\ \tau_y \\ \tau_z \end{bmatrix} \tag{9}$$

A. Thrust limits

Our control strategy differs from that of a standard quadcopter in the computation of input saturations. Normally, the minimum and maximum thrust produced by an individual propeller is bounded by the performance limitations of the motor driving it. For our vehicle, however, additional bounds on the individual thrusts are imposed in order to prevent the arms from folding during regular flight. These bounds keep the vehicle in the unfolded configuration, meaning that existing quadcopter controllers can be used with only a minor reduction in performance due to a more limited range of control inputs. The reduction in the available thrust range is governed by the spring forces $\boldsymbol{f}_{s_i}$ and the linear and angular acceleration of the central body.

Rather than imposing limits on the individual thrust forces, we limit the desired total thrust f_Σ and desired body torques (τ_x, τ_y, τ_z) such that (9) produces thrust forces that will keep the arms unfolded. The vehicle will remain in the unfolded configuration if the following inequality is satisfied and assuming $\boldsymbol{\omega}_{BE}$ is small such that centrifugal forces are negligible. Let $\boldsymbol{J}_\Sigma^C$ be the mass moment of inertia of the entire vehicle taken at the center of mass of the vehicle, $\boldsymbol{d}_{CA_i}^{A_i}$ be the displacement of the center of mass of the vehicle from arm i, and $\tau_s = \boldsymbol{y}_{A_i}^{A_i} \cdot S(\boldsymbol{d}_{M_i H_i}^{A_i})(-\boldsymbol{f}_{s_i}^{A_i})$ be the torque exerted by spring i on arm i. The double subscript $\boldsymbol{J}_{yy}$ denotes the (2, 2) element of matrix $\boldsymbol{J}$. A derivation of this expression can be found in the online appendix [15].

$$|c_f| f_\Sigma - |c_{xy}| \max(|\tau_x|, |\tau_y|) - |c_z||\tau_z| \geq |c_s| \tag{10}$$

where

$$|c_f| = \frac{1}{4} - \frac{d_{A_i H_i,x}^{A_i}}{d_{P_i H_i,x}^{A_i}} \frac{m_A}{4m_A + m_B} \tag{11}$$

$$|c_{xy}| = \frac{1}{2l_{PB}} - \frac{1}{d_{P_i H_i,x}^{A_i}} \widetilde{J}_{A_i,yy}^{A_i} (\boldsymbol{J}_{\Sigma,yy}^{C})^{-1} \tag{12}$$

$$|c_z| = \frac{1}{4} |\kappa_{p_i}|^{-1}, \quad |c_s| = \frac{1}{d_{P_i H_i,x}^{A_i}} \tau_s \tag{13}$$

and

$$\widetilde{J}_{A_i,yy}^{A_i} = \left(\boldsymbol{J}_{A_i}^{A_i} + m_A S(\boldsymbol{d}_{A_i H_i}^{A_i}) S(\boldsymbol{d}_{CA_i}^{A_i}) \right)_{yy} \tag{14}$$

By converting the bounds on the thrust forces to bounds on the control inputs, an intuitive method for dealing with input saturation can be implemented. Similar to the method presented in [16], we propose a hierarchical reduction of the control inputs in the event that (10) is not satisfied. First, the magnitude of the yaw torque τ_z is reduced until the bound is satisfied or $\tau_z = 0$. Next, f_Σ is increased until the bound is satisfied or it reaches the maximum total thrust the propellers can produce. If the maximum total thrust is reached, then the roll and/or pitch torques are reduced until the bound is satisfied. In practice, however, decreasing the roll and/or pitch torques in order to prevent the arms from folding is seldom necessary due to the magnitude of c_{xy} relative to the other terms.

B. Configuration transition

In order to transition between the unfolded and folded configurations, the commanded thrust for each motor is set to a value low enough to allow the spring force to overcome the thrust force produced by the motor. Similarly, in order to transition between the folded and unfolded configurations, sufficiently high thrust forces are commanded such that the thrust forces overcome the spring forces, causing the arms to unfold.

IV. Design

The vehicle design departs from the design of a standard quadcopter in the inclusion of an passive hinge where the arms attach to the central body and the use of constant force springs to pull the arms closed when low thrusts are produced by the motors. The position of the hinge is chosen such that the size of the vehicle is minimized in the folded configuration. For the experimental vehicle, the displacement of hinge 1 from the center of mass of the body is $\boldsymbol{d}_{H_1 B}^{B} = (5\,\text{cm}, 0\,\text{cm}, -1.2\,\text{cm})$.

The attachment points and force of the constant-force springs are chosen in order to minimize the time required to transition from the unfolded configuration to the folded configuration and back. The spring-related parameters are constrained based on (10) such that the total thrust required to keep the arms in the unfolded configuration is no more than 70% of the total thrust required to hover. Thus, a constrained optimization problem can be used to determine the location of the spring mounting points M_i on the arm, S_i on the central body, and the magnitude

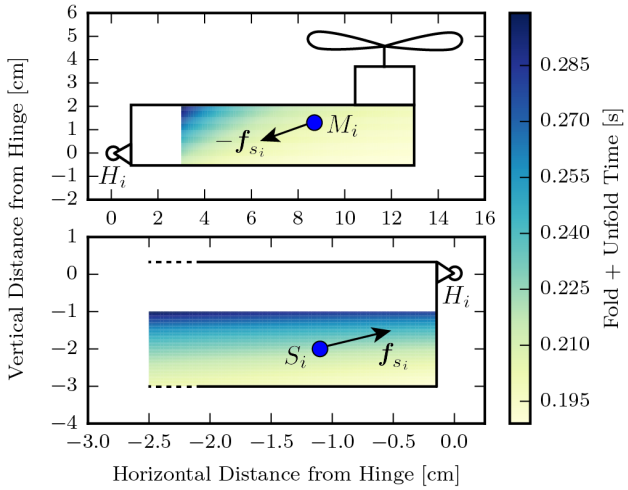

Fig. 3. Simulated configuration transition times for a 5.4 N spring with different attachment positions. Top: the arm mounting point M_i is varied given a constant body mounting point S_i. Bottom: the body mounting point S_i is varied given a constant arm mounting point M_i. All displacements are with respect to the hinge position. The spring attachment positions used on the experimental vehicle are marked with blue dots. Configuration transition times were computed using a dynamic simulation of the vehicle in free-fall starting with the arms unfolded.

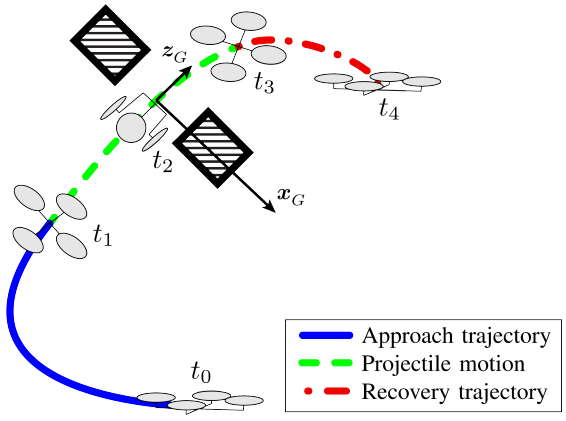

Fig. 4. The approach trajectory starts from rest at time t_0 and ends at a desired launch state at time t_1, at which time the vehicle starts to transition to the folded configuration. The launch state is chosen such that the vehicle will finish folding and travel through the gap in projectile motion at time t_2. The vehicle finishes transitioning to the unfolded configuration at time t_3 and then follows a recovery trajectory, coming to rest at time t_4.

of the spring force f_{s_i}. Figure 3 shows how the locations of M_i and S_i were chosen given f_{s_i}. The experimental vehicle was designed with the following spring parameter choices: $\boldsymbol{d}^{A_i}_{M_iH_i} = (-8.3\,\text{cm}, 0\,\text{cm}, -1.1\,\text{cm})$, $\boldsymbol{d}^{B}_{S_1H_1} = (-1.1\,\text{cm}, 0\,\text{cm}, -2\,\text{cm})$, and $f_{s_i} = 5.4\,\text{N}$.

The bounds on the control inputs given by (10) determine the ideal mass distribution between the central body and the four arms as well as the ideal distance of the thrust axis of each propeller from its respective hinge such that the available range of control inputs $(f_\Sigma, \tau_x, \tau_y, \tau_z)$ is maximized. The second term of (11) implies that decreasing the mass of the arms with respect to the total mass of the vehicle will result in a lower total thrust required to keep the arms unfolded and thus maintain a higher vehicle agility. Increasing the distance of the propellers from the hinges $\boldsymbol{d}^{A_i}_{P_iH_i,x}$ will also lower the thrust required to keep the arms unfolded. Finally, $|c_s|$ can be decreased by lowering the magnitude of the spring force $\boldsymbol{f}_{s_i}$ or changing the attachment locations of the spring such that a lower torque is produced by the spring in the unfolded configuration.

V. Gap Traversing Trajectory Generation

The gap crossing maneuver consists of three major stages: an approach trajectory, projectile motion, and a recovery trajectory. Figure 4 depicts the entire maneuver. Similar to [3], we define the end state of the approach trajectory based on the desired motion through the gap. In contrast to [3], our vehicle enters projectile motion during gap traversal, and thus requires a different set of constraints on the state of the vehicle at the end of the approach trajectory. Furthermore, we extend the minimum jerk trajectory generation method presented in [17] by including constraints on the angular velocity of the vehicle at time t_1 and incorporating feedforward terms to compensate for drag effects while tracking the trajectory.

The gap is defined by a position, $\boldsymbol{d}^E_{GE}$, and a unit vector pointing in the desired direction of travel through the gap, $\boldsymbol{z}_G$. The gap-fixed frame G is defined such that $\boldsymbol{z}_G$ points in the desired direction of motion through the gap and $\boldsymbol{y}_G$ is perpendicular to the direction of gravity. Given the position and orientation of the gap, we seek to find feasible trajectories using the method presented in [17] that result in the vehicle passing through the center of the gap with a positive velocity in the $\boldsymbol{z}_G$ direction at time t_2:

$$\boldsymbol{d}^G_{BE}(t_2) = \boldsymbol{d}^G_{GE}, \qquad \dot{\boldsymbol{d}}^G_{BE}(t_2) = (0,\ 0,\ v_2) \tag{15}$$

Let the time required to transition into the folding configuration be $t_{fold} = (t_2 - t_1)$. The desired position and velocity of the vehicle at time t_1 can then be found by propagating (15) backward through the projectile dynamics of the vehicle. We also impose a constraint on the acceleration direction of the vehicle at time t_1 such that the projected area of the vehicle onto the gap plane is minimized. This corresponds to constraining the thrust direction $\boldsymbol{z}_B$ to be coincident with the gap direction $\boldsymbol{z}_G$ during the projectile portion of the trajectory. We extend the work of [17] by specifying a jerk of zero at time t_1 at the expense of leaving the initial position of the approach trajectory to be free. Because the angular velocity of the vehicle is determined by the jerk, this constraint forces the desired angular velocity of the vehicle to be zero at time t_1, minimizing the rotation of the vehicle while traversing the gap between times t_1 and t_3. These constraints on the state of the vehicle at time t_1 are written in the gap frame as:

$$\begin{aligned}
&\dddot{\boldsymbol{d}}^G_{BE}(t_1) = (0,0,0), \quad \ddot{\boldsymbol{d}}^G_{BE}(t_1) = (0,0,a_1)\\
&\dot{\boldsymbol{d}}^G_{BE}(t_1) = (0,\ 0,\ v_2) - t_{fold}\boldsymbol{R}^{GE}\boldsymbol{g}^E\\
&\boldsymbol{d}^G_{BE}(t_1) = \boldsymbol{d}^G_{GE} - t_{fold}\dot{\boldsymbol{d}}^G_{BE}(t_1) - \frac{1}{2}t^2_{fold}\boldsymbol{R}^{GE}\boldsymbol{g}^E
\end{aligned} \tag{16}$$

We assume the vehicle is in hover at time t_0, meaning that the velocity of the vehicle set to zero and the acceleration is in the opposite direction of gravity. The position of the vehicle at time t_0 is left free. These constraints on the state of the vehicle at time t_0 are written in the gap frame as:

$$\ddot{\boldsymbol{d}}^G_{BE}(t_0) = \boldsymbol{R}^{GE}(0, 0, a_0), \quad \dot{\boldsymbol{d}}^G_{BE}(t_0) = (0,\ 0,\ 0) \quad (17)$$

Given the constraints in (16) and (17) we generate many different minimum jerk trajectories by varying the velocity through the gap v_2, the magnitude of acceleration at the moment of folding a_1, the initial acceleration magnitude a_0, and the time required to execute the trajectory $t_1 - t_0$. The trajectory that maximizes v_2 with the minimum average jerk is selected in order minimize the time spent in projectile motion. Trajectories that cross the $\boldsymbol{x}_G$-$\boldsymbol{y}_G$ plane, go outside a specified work area, or exceed constraints on the maximum total thrust and angular velocity are rejected. In order to validate that a recovery trajectory exists where the vehicle will stay within the work area and on the opposite side of the gap, a recovery trajectory between times t_3 and t_4 is generated using the methods presented in [17].

VI. Experimental Results

The experimental vehicle shown in Figure 1 has a mass of $940\,\mathrm{g}$ and moments of inertia of $4 \times 10^{-3}\,\mathrm{kg\,m^2}$ and $8 \times 10^{-3}\,\mathrm{kg\,m^2}$ about the $\boldsymbol{x}_B$ and $\boldsymbol{z}_B$ axes respectively. The input bounds given by (10) result in an increase of the minimum total thrust from $0\,\mathrm{N}$ to $6.45\,\mathrm{N}$ when the desired body torques are zero, and result in a reduction of the maximum yaw torque from $0.13\,\mathrm{N\,m}$ to $0.03\,\mathrm{N\,m}$ when the vehicle is hovering. The maximum roll/pitch torques while in hover exceeded the maximum roll/pitch torques that the propellers can produce, resulting in no reduction in the ability of the vehicle to maneuver in roll/pitch during hover.

Note that the decrease in the range of control inputs is heavily dependent on the spring force $\boldsymbol{f}_{s_i}$. In this work we have chosen the largest possible magnitude $\boldsymbol{f}_{s_i}$ so that the vehicle can transition between configurations quickly, resulting in a minimum total thrust close to 70% of the thrust produced at hover and a significant reduction in the yaw authority of the vehicle. If a rapid transition into the folded configuration is not required, weaker springs (or no springs) could be used, greatly increasing the range of feasible control inputs. Section IV describes how the constraint on the minimum total thrust at hover can be incorporated into the design.

A. Configuration transition time

A numeric simulation was conducted using the dynamics presented in Section II in order to determine the time required to transition between configurations. Assuming the vehicle starts from rest in the unfolded configuration with $f_{p_i} = 0\,\mathrm{N}$, the simulated vehicle requires $0.15\,\mathrm{s}$ to transition to the folded configuration, and requires $0.09\,\mathrm{s}$ to transition back to the unfolded configuration with $f_{p_i} = 4\,\mathrm{N}$. The experimental folding and unfolding times were measured using an onboard accelerometer to detect the collisions of the arms with central body at the end of each configuration transition. Figure 5 shows an example of the vehicle hovering, folding, unfolding, and then returning to hover. The time required to fold and unfold were found to be $0.44\,\mathrm{s}$ and $0.15\,\mathrm{s}$ respectively.

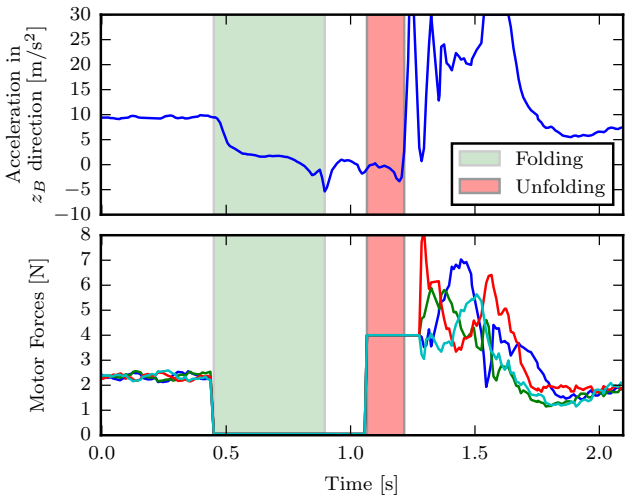

Fig. 5. The accelerometer signal is used to detect when the arms collide with the central body in order to measure the time required to transition between configurations. The start of the transition to the folded and unfolded configurations are defined by the times at which thrust commands of zero and $4\,\mathrm{N}$ respectively are sent to each motor. The arms take approximately $0.44\,\mathrm{s}$ to fold and $0.15\,\mathrm{s}$ to unfold.

We hypothesize that the discrepancy between the theoretical and experimental configuration transition times can be explained by the lack of friction in our system model and/or by unmodeled motor dynamics. For example, we assume that the propellers are able to instantaneously change the amount of thrust they produce, but in reality the motors require some amount of time to bring the propellers to a stop when transitioning into the folded configuration. This means that the propellers continue to produce some amount of thrust while folding, which the theoretic folding transition time does not account for.

B. Gap traversal

The method presented in Section V was used to generate an approach trajectory that brings the vehicle to a state such that it will traverse the desired gap while folded. The generated trajectory was tracked without the gap present, and the position of the gap was then adjusted to match the true path of the vehicle. Such iterative methods are unnecessary if the vehicle is able to track the desired trajectory without error. However, highly accurate trajectory tracking is outside the scope of this work.

Figure 6 shows the vehicle flying through a gap oriented at 90° from the vertical using the iterative method described above (other gap orientations are similarly traversed). Figure 7 shows a head-on view of the vehicle as it flies through the gap, showing that the vehicle must be in the folded configuration to pass through. The vehicle transitions back into the unfolded configuration after a predefined amount

Fig. 6. The vehicle was flown through a vertical gap by transitioning to the folded configuration, passing through the gap, unfolding, and recovering on the other side (from left-to-right in the image). The gap traversal maneuver was repeated several times without collision. Video of experiments: `https://youtu.be/MSvoQT__c9U`

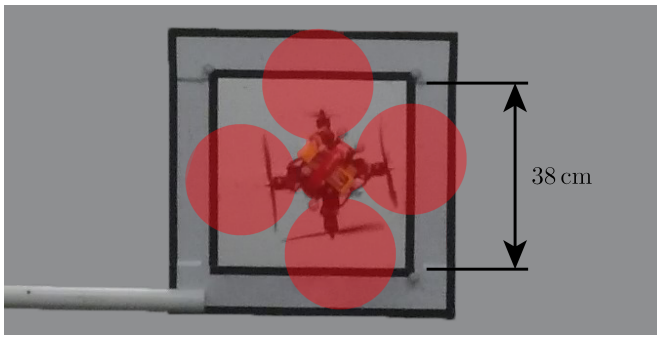

Fig. 7. Head-on view of gap traversal with the outline of the vehicle in the unfolded configuration show in red. The vehicle cannot fit through the gap in the unfolded configuration in any orientation, but is small enough to traverse the gap in the folded configuration.

time by commanding a constant thrust from each motor for a short period and then enforcing the bounds from (10) during the recovery trajectory.

Figure 8 shows the position, velocity, pitch, and pitch rate of the vehicle during the maneuver shown in Figure 6. Because the approach trajectory is constrained to end at time t_1 with zero angular velocity and a thrust direction in the z_G direction, the pitch angle and pitch rate of the vehicle remain at approximately 90° and $0\,\mathrm{rad\,s^{-1}}$ respectively between times t_1 and t_3.

VII. Conclusion

In this paper we have presented a novel quadcopter design that utilizes passive rotary joints in order to change shape mid-flight without the use of additional actuators. The dynamics of such a vehicle were derived, and bounds on the total thrust and body torques exerted by the propellers such that the vehicle remains in the unfolded configuration were presented. The design of the vehicle was chosen such that while the bounds on the control inputs are satisfied, existing quadcopter controllers and trajectory generation methods can

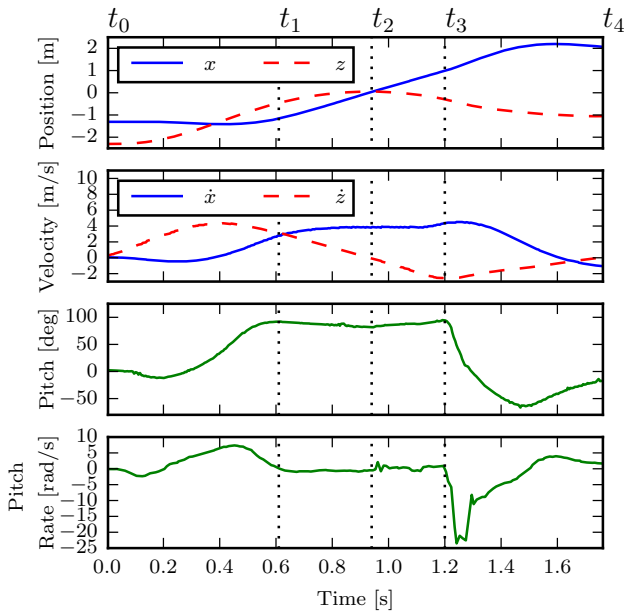

Fig. 8. Estimated state of the vehicle during the gap crossing maneuver shown in Figure 6. The vehicle tracks the approach trajectory starting at t_0, and begins folding at t_1. At t_2 the vehicle passes through the gap. From t_3 to t_4 the vehicle recovers from the maneuver and comes to rest. The position of the vehicle is given relative to the position of the gap. The coordinates x and z are defined to point horizontally and upwards, respectively.

be used. Furthermore, the design requires only a relatively small increase in mechanical complexity compared to other aerial morphing vehicles.

The vehicle was shown performing a gap traversal maneuver, requiring a change of shape and aggressive launch and recovery maneuvers. Although a motion capture system was used in this paper to localize the vehicle and gap with high precision, the fundamental design of the vehicle does not rely on such high precision localization. The ability of the vehicle to reduce its size during flight still reduces the probability of collision with an obstacle when less precise localization methods are used.

In future designs the size of the vehicle in the folded configuration could be further reduced by allowing the disks swept by the propellers to intersect in the folded configuration. Because each propeller counter-rotates relative to its two neighbors, if all four propellers are kept at similar speeds while folding and unfolding the speed of the blades relative to each other would be small and any collisions between blades would be minor.

Acknowledgement

The authors would like to thank Martin Xu and Christian Castaneda for their help with the design and construction of the vehicle. The experimental testbed at the HiPeRLab is the result of contributions of many people, a full list of which can be found at `hiperlab.berkeley.edu/members/`. This material is based upon work supported by the National Science Foundation Graduate Research Fellowship under Grant No. DGE 1752814.

REFERENCES

[1] C. Richter, A. Bry, and N. Roy, "Polynomial trajectory planning for aggressive quadrotor flight in dense indoor environments," in *Robotics Research*. Springer, 2016, pp. 649–666.

[2] D. Mellinger, N. Michael, and V. Kumar, "Trajectory generation and control for precise aggressive maneuvers with quadrotors," *The International Journal of Robotics Research*, vol. 31, no. 5, pp. 664–674, 2012.

[3] D. Falanga, E. Mueggler, M. Faessler, and D. Scaramuzza, "Aggressive quadrotor flight through narrow gaps with onboard sensing and computing using active vision," in *Robotics and Automation (ICRA), 2017 IEEE International Conference on*. IEEE, 2017, pp. 5774–5781.

[4] N. Zhao, Y. Luo, H. Deng, and Y. Shen, "The deformable quadrotor: Design, kinematics and dynamics characterization, and flight performance validation," in *Intelligent Robots and Systems (IROS), 2017 IEEE/RSJ International Conference on*. IEEE, 2017, pp. 2391–2396.

[5] A. Desbiez, F. Expert, M. Boyron, J. Diperi, S. Viollet, and F. Ruffier, "X-morf: a crash-separable quadrotor that morfs its x-geometry in flight," in *RED UAS 2017-Research, Education and Development of Unmanned Aerial Systems*, 2017.

[6] C. Hintz, C. Torno, and L. R. G. Carrillo, "Design and dynamic modeling of a rotary wing aircraft with morphing capabilities," in *Unmanned Aircraft Systems (ICUAS), 2014 International Conference on*. IEEE, 2014, pp. 492–498.

[7] V. Riviere, A. Manecy, and S. Viollet, "Agile robotic fliers: A morphing-based approach," *Soft Robotics*, 2018.

[8] M. Ryll, H. H. Bülthoff, and P. R. Giordano, "First flight tests for a quadrotor uav with tilting propellers," in *Robotics and Automation (ICRA), 2013 IEEE International Conference on*. IEEE, 2013, pp. 295–302.

[9] I. Schiffner, H. D. Vo, P. S. Bhagavatula, and M. V. Srinivasan, "Minding the gap: in-flight body awareness in birds," *Frontiers in zoology*, vol. 11, no. 1, p. 64, 2014.

[10] M. Di Luca, S. Mintchev, G. Heitz, F. Noca, and D. Floreano, "Bioinspired morphing wings for extended flight envelope and roll control of small drones," *Interface focus*, vol. 7, no. 1, p. 20160092, 2017.

[11] S. Mintchev, L. Daler, G. L'Eplattenier, L. Saint-Raymond, and D. Floreano, "Foldable and self-deployable pocket sized quadrotor," in *Robotics and Automation (ICRA), 2015 IEEE International Conference on*. IEEE, 2015, pp. 2190–2195.

[12] P. Pounds, R. Mahony, P. Hynes, and J. M. Roberts, "Design of a four-rotor aerial robot," in *Proceedings of the 2002 Australasian Conference on Robotics and Automation (ACRA 2002)*. Australian Robotics & Automation Association, 2002, pp. 145–150.

[13] P. H. Zipfel, *Modeling and Simulation of Aerospace Vehicle Dynamics*, 2nd ed. American Institute of Aeronautics and Astronautics, 2007.

[14] N. Bucki and M. W. Mueller, "Improved quadcopter disturbance rejection using added angular momentum," in *Intelligent Robots and Systems (IROS), 2018 IEEE/RSJ International Conference on*. IEEE, 2018.

[15] ——. (2018) Online appendix to "design and control of a passively morphing quadcopter". [Online]. Available: http://mwm.im/link/FoldingArms

[16] M. Faessler, D. Falanga, and D. Scaramuzza, "Thrust mixing, saturation, and body-rate control for accurate aggressive quadrotor flight," *IEEE Robotics and Automation Letters*, vol. 2, no. 2, pp. 476–482, 2017.

[17] M. W. Mueller, M. Hehn, and R. D'Andrea, "A computationally efficient motion primitive for quadrocopter trajectory generation," *IEEE Transactions on Robotics*, vol. 31, no. 6, pp. 1294–1310, 2015.